Zinc Batteries

Engineering Nanoscale Interfacial Solvation Inner-Outer Configuration via Multi-Group Synergy for Practical Zinc Batteries

Yeguang Zhang, Zichang Zhang, Haozhen Dou,* Zhiyuan Bai, Jiabin Zou, Yujie Wang, Feihu Li, Peng Wang, Jie Zhang, Mi Xu,* and Zhongwei Chen*

Abstract: Rational design of interfacial solvation structures in electric double layer (EDL) remains a critical challenge for aqueous zinc metal batteries (AZMBs). Herein, an efficient multi-group synergy strategy has been proposed to precisely regulate the interfacial solvation structure at nanoscale, which affords long-lifespan AZMBs under high depth of discharge (DOD) and low temperature. Through combined in situ experiments and theoretical simulations, we demonstrate trace multifunctional group biomolecular additive cannot alter electrolyte solvation structure, but contributes to formation of the positively charged Zn^{2+} solvation shell in outer Helmholtz layer (OHL) and additive-involved and H_2O/anion-less solvation shell in inner Helmholtz layer (IHL). This synergistic configuration enables an organic-inorganic hybrid interface that simultaneously suppresses hydrogen evolution, accelerates desolvation, offers pH buffering capacity, and regulates Zn^{2+} deposition orientation. Zn anodes deliver high coulombic efficiency of 99.65%, long-lifespan over 6500 h, and stable operation under low temperature of −20 °C and high DOD of 85.4%. Furthermore, under practical condition of high mass loading (27 mg cm^{-2}) and limited N/P ratio of 3.5, Zn||VO$_2$ battery delivers a superhigh surface capacity of 8.1 mAh·cm^{-2} and remains stable over 800 cycles, and pouch batteries can stably operate for almost 500 cycles.

Introduction

Advanced electrochemical energy storage technologies are highly important and urgently needed for the application of clean energy toward sustainable energy future.[1,2] In this scene, aqueous zinc metal batteries (AZMBs) have aroused significant interest and are endowed with great expectations as next-generation battery technology for large-scale energy storage, which offer several advantages over traditional lithium-ion batteries, such as superior safety, cost-effectiveness, and eco-friendliness.[3,4] Particularly, Zn metal anode is featured with abundant supply, the low redox potential (−0.76 V versus standard hydrogen electrode) and high theoretical capacity (820 mAh·g^{-1}). However, Zn metal anode still faces the challenges of serious hydrogen evolution reaction (HER), corrosion and dendrite growth in aqueous electrolytes, resulting in poor cycling stability and low coulombic efficiency (CE).[5,6] These critical challenges are primarily attributed to the abundant thermodynamically-active water molecules in the Zn^{2+} solvation shell and electric double layer (EDL) of aqueous electrolytes.[7–9] Therefore, the regulation of solvation structure or electrode interface is crucial for realizing the high-performance of AZMBs.

Electrolyte engineering is the straightforward methodology to modify the solvation structure and electrode interface.[10,11] One approach focused on developing water-in-salt electrolytes, eutectic electrolytes, or organic hybrid electrolytes by introducing metal salt, organic cosolvent, or organic ligand into aqueous electrolyte, which can participate in the Zn^{2+} solvation coordination and regulate Zn^{2+} solvation shell of bulk electrolyte, thus minimizing the solvated H_2O and suppressing H_2O-induced parasitic reactions.[12–14] However, this approach always lies in high concentration of metal salt or organic solvents, imposing the concern of decreased ionic conductivity, increased cost and potential safety risk.[15] Alternatively, inexhaustible functional additives are developed to tailor interface properties, and these additives cannot alter the solvation structure of bulk electrolyte due to their trace content or steric hindrance effect.[16,17] However, these additives can decrease interface active H_2O and regulate Zn^{2+} deposition due to the preferential adsorption toward Zn anode, where the enhancement of battery performance has been understood by different perspectives.[18,19] For example, a series of metal cations (Ga^{3+}, Ce^{3+}, La^{3+}, and Y^{3+}) have been proposed to guide even Zn^{2+} deposition via dynamical electrostatic shielding,[20–25] while some thiol compounds and fluorinated organic compounds can induce in situ formation of self-assembled protection layer or solid electrolyte interface (SEI) for improving interfacial stability.[26–28] More generally, many additives with high donor number or high adsorption

[*] Y. Zhang, Z. Zhang, J. Zou, F. Li, P. Wang
School of Chemical Engineering, Zhengzhou University, Zhengzhou 450001, China

H. Dou, Z. Bai, Y. Wang, J. Zhang, M. Xu, Prof. Z. Chen
Power Battery and Systems Research Center, State Key Laboratory of Catalysis, Dalian Institute of Chemical Physics, Chinese Academy of Sciences, Dalian 116023, China
E-mail: haozhen@dicp.ac.cn
xumi@dicp.ac.cn
zwchen@dicp.ac.cn

☐ Additional supporting information can be found online in the Supporting Information section

capability can effectively tailor EDL for decreasing interfacial active water and promoting the desolvation process, thereby enhancing the reversibility of the Zn anode.[29,30] Actually, additive aggregation within EDL and the EDL reconstruction results in the obvious evolution of Zn^{2+} solvation configuration from bulk electrolyte to EDL, which plays an important role in Zn^{2+} interfacial migration and desolvation, the structure and chemistry of SEI, as well as final reduction and deposition on the Zn anode, especially when the battery is operated at high depth of discharge (DOD) and low temperature.[31–33] Compared widely acknowledged solvation structure of bulk electrolyte, the interfacial solvation structure has been seldom investigated for AZMBs.[34–38] Therefore, understanding the interfacial solvation structure within EDL and developing the related regulation strategy are imperative but challenging for high-performance AZMBs.[39–41]

Herein, this work clearly elucidates the interfacial solvation structure of aqueous electrolyte, and proposes an efficient multi-group synergy strategy for regulating interfacial solvation structure in EDL for AZMBs, which significantly boosting the reversibility of Zn anode under high DOD and low temperature.[42,43] Based on cost-effective and environmentally friendly electrolyte design principles, biomolecule D-pantothenol (DP) with multiple types of functional groups is selected as an electrolyte additive prototype, which can significantly reconstruct EDL and precisely regulate interfacial solvation structure even under extremely low concentration of 0.05 mol L^{-1}.[44,45] Experimental investigations and theoretical calculations demonstrate trace DP additive do not alter the solvation structure of bulk electrolyte. DP molecules preferentially adsorb on the Zn anode and deliver gradient distribution from the inner Helmholtz layer (IHL) to outer Helmholtz layer (OHL), which decreases active water in EDL and changes the distribution of Zn^{2+} and SO_4^{2-}.[46–48] Remarkably, the interfacial interactions between $H^+/H_2O/Zn^{2+}$ and multifunctional groups of DP reorganize the solvation shell in EDL, where positively charged Zn^{2+} solvation shell in OHL and additive-involved and H_2O/anion-less solvation shell in IHL are constructed. The unique interfacial solvation structure prompts the formation of stable organic-inorganic hybrid SEI, accompanied by the decreased activation energy, improved Zn^{2+} transference number and robust pH buffering capacity. Moreover, compact and dense Zn deposition with enhanced orientation of (002) crystal plane is achieved and H_2O related parasitic reactions is effectively suppressed.[49,50] Consequently, Zn‖Zn symmetric battery demonstrates stable cycling performance, maintaining more than 6500 h and sustaining over 550 h even at a high DOD of 85.4% and over 1200 h at −20 °C. Furthermore, the Zn‖PANI (polyaniline) battery retains 80% of capacity after 5300 cycles, and Zn‖VO$_2$ battery delivers a superhigh surface capacity of 8.1 mAh·cm^{-2} and remains stable over 800 cycles under practical condition of high mass loading (27 mg cm^{-2}) and limited N/P ratio (3.5), and pouch batteries can stably operate for almost 500 cycles, exceeding the most reported pouch batteries. The pioneering attempt of interfacial solvation engineering provides a new perspective for developing high-performance batteries.

Results and Discussion

Electrolyte Design and Solvation Structure of Bulk Electrolyte

As for conventional aqueous electrolyte, Zn^{2+} is hydrated by H_2O molecules to form the representative solvation shell of $[Zn(H_2O)_6]^{2+}$ in the bulk electrolyte, and H_2O molecules are orientationally adsorbed onto Zn anode surface to form a water-rich inner EDL, closely followed by an outer EDL populated with hydrated Zn^{2+} solvation shell and counter anion. The plenty of active H_2O in the solvation shell and EDL results in the severe parasitic reactions and rampant dendrite formation (Figure 1a). DP, also known as Vitamin B5, integrates three hydroxyl groups, carbonyl group, imine group and two hydrophobic methyl groups, which is characterized by low cost, biodegradability, and non-toxicity to the human body, being widely used in pharmaceuticals, food and cosmetics.[51,52] As highlighted by electrostatic potential map (Figure S1), DP possesses multiple positive and negative charge sites, which affords the multi-group synergy regulation for electrolyte and electrode interface. After introduction of DP in the aqueous electrolyte, the solvation structure of bulk electrolyte remains unchanged, but DP molecules are preferentially adsorbed on the Zn anode and reconstruct EDL structure on the Zn anode interface. The gradient distribution of DP from the IHL to outer OHL decreases H_2O molecules in EDL and also changes the distribution and concentration of Zn^{2+} and SO_4^{2-}, which alters the interfacial Zn^{2+} solvation shell in EDL, thus inducing stable organic-inorganic hybrid SEI and fostering collaborative interface functions (Figure 1b).[53–55] As a consequence, H_2O related parasitic reactions and dendrite growth are effectively suppressed, thus boosting electrochemical performance of AZMBs.

A family of ZS-DP electrolytes are prepared by dissolving DP into 2 M $ZnSO_4$ electrolyte at different concentrations of 0.05, 0.1, and 0.5 mol L^{-1}, respectively, which are denoted as ZS-0.05DP, ZS-0.1DP, and ZS-0.5DP (Figure S2). 2 M $ZnSO_4$ aqueous electrolytes is abbreviated as ZS and used as control experiment. As revealed by electrochemical impedance spectroscopy (EIS), the ZS-DP electrolytes show high ionic conductivity, but high DP concentration slightly decreases the ion conductivity due to the enhanced viscosity (Figures S3 and S4). Especially, ZS-0.05DP electrolyte almost maintains the same ionic conductivity with ZS due to the extremely low concentration. Moreover, ZS-0.05DP electrolyte still maintains the acceptable ion conductivity at low temperature of −20 °C. Notably, ZS-DP electrolytes remain the high safety, as confirmed by ignition test (Figure S5). Interestingly, the addition of DP reduces the freezing point of electrolyte to −25 °C despite the small amount of DP, thus enabling the battery to operate under low temperature (Figure S6).

^{1}H nuclear magnetic resonance (^{1}HNMR), Raman spectroscopy, and attenuated total reflection Fourier-transform infrared (ATR-FTIR) spectroscopy are performed to investigate the structure and intermolecular interactions of ZS-DP electrolytes.[56–58] In the ^{1}HNMR spectra, the chemical shift of H_2O gradually moves to down-field with the addition of DP, which indicates the formation of hydrogen bonds between DP
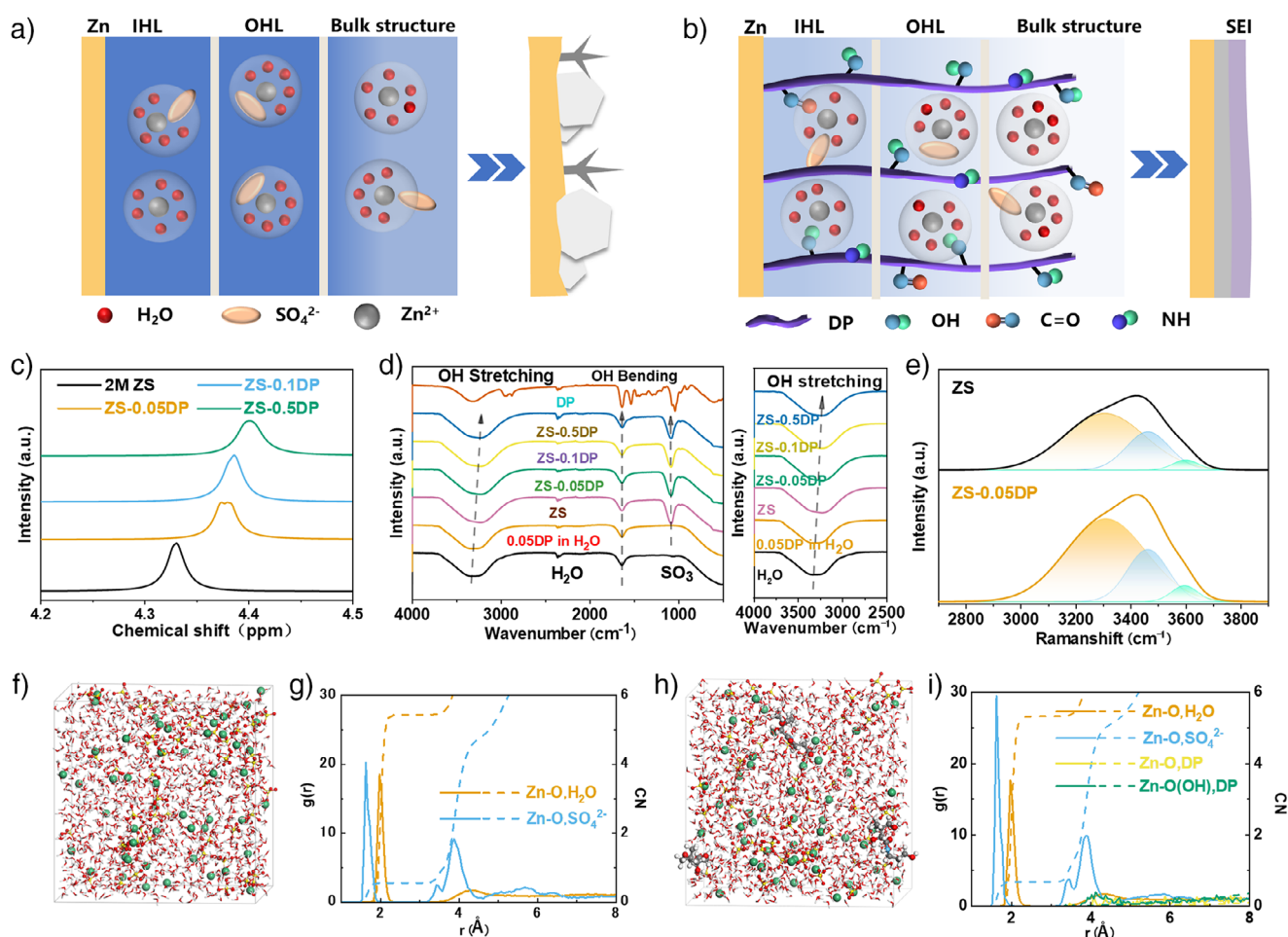
Figure 1. Electrolyte design and intermolecular interaction analysis. a) Unchanged solvation structure of bulk electrolyte and within EDL, where abundant thermodynamically-active water molecules induce severe parasitic reactions and dendrite growth. b) Regulation of the interfacial solvation structure via multifunctional group biomolecular additive, which contributes to highly reversibility of Zn anode with hybrid SEI. c) ^{1}HNMR spectroscopy characterization of ZS-DP electrolytes. d) ATR-FTIR spectra of ZS-DP electrolytes and the highlighted OH stretching vibration region. e) Deconvolution of OH stretching vibration in Raman spectra of ZS-DP electrolytes. f), g) 3D snapshot of MD simulations for ZS electrolyte, and RDF and coordination number collected from MD simulations. h), i) 3D snapshot of MD simulations for ZS-DP electrolyte, and RDF and coordination number collected from MD simulations.

and H$_2$O in ZS-DP electrolytes (Figure 1c). Compared with ZS electrolyte, the peak of ZS-DP electrolytes is broadened, which is attributed to the formation of multiple types of hydrogen bonds between H$_2$O and multifunctional groups of DP. As further confirmed by ATR-FTIR spectra (Figure 1d), the noticeable red-shift from 3334 to 3227 cm^{-1} is observed for OH stretching vibration peak with the gradual increase of DP concentration. Simultaneously, the peak corresponding to OH bending vibration also shifts from 1637 to 1632 cm^{-1}, which suggests the original hydrogen bond network among H$_2$O molecules are disrupted. Additionally, the stretching vibration peak of SO$_4^{2-}$ shows no shift, indicating that the solvation structure of Zn^{2+} remains unchanged. Raman spectra further confirm the changes in hydrogen bond interactions of electrolytes (Figure S7). The O-H stretching vibration of water in the range of 3000–3700 cm^{-1} can be convoluted into three components, with peaks at ~3230, ~3480, and ~3620 cm^{-1} corresponding to strong hydrogen bonds, weak hydrogen bonds, and non-hydrogen bonds, respectively. The peak

intensity of ZS-0.05DP electrolyte and proportion of strong hydrogen bond intensify in relative to ZS electrolyte, which confirms more and stronger hydrogen-bond interactions are formed in ZS-DP electrolyte, thus reducing thermodynamic activity of free and solvated H$_2$O (Figure 1e and Table S1). Moreover, the peak at 982 cm^{-1} in Raman spectra represents SO$_4^{2-}$ and remains unshifted, which indicates that DP does not affect the Zn^{2+} solvation structure, being consistent with ATR-FTIR.

The Zn^{2+} solvation structure of bulk electrolyte is analyzed by molecular dynamics (MD) simulation. As highlighted by the 3D snapshot of of ZS and ZS-0.05 DP electrolyte, the trace DP molecules show negligible influence on the electrolyte nanostructure such as component distribution and agglomeration behavior (Figure 1f,h). The radial distribution functions (RDFs) and coordination numbers (CNs) further indicate DP molecules donnot enter into Zn^{2+} solvation shell, and the average CNs of H$_2$O and SO$_4^{2-}$ in the first Zn^{2+} solvation shell of ZS and ZS-DP electrolytes are nearly
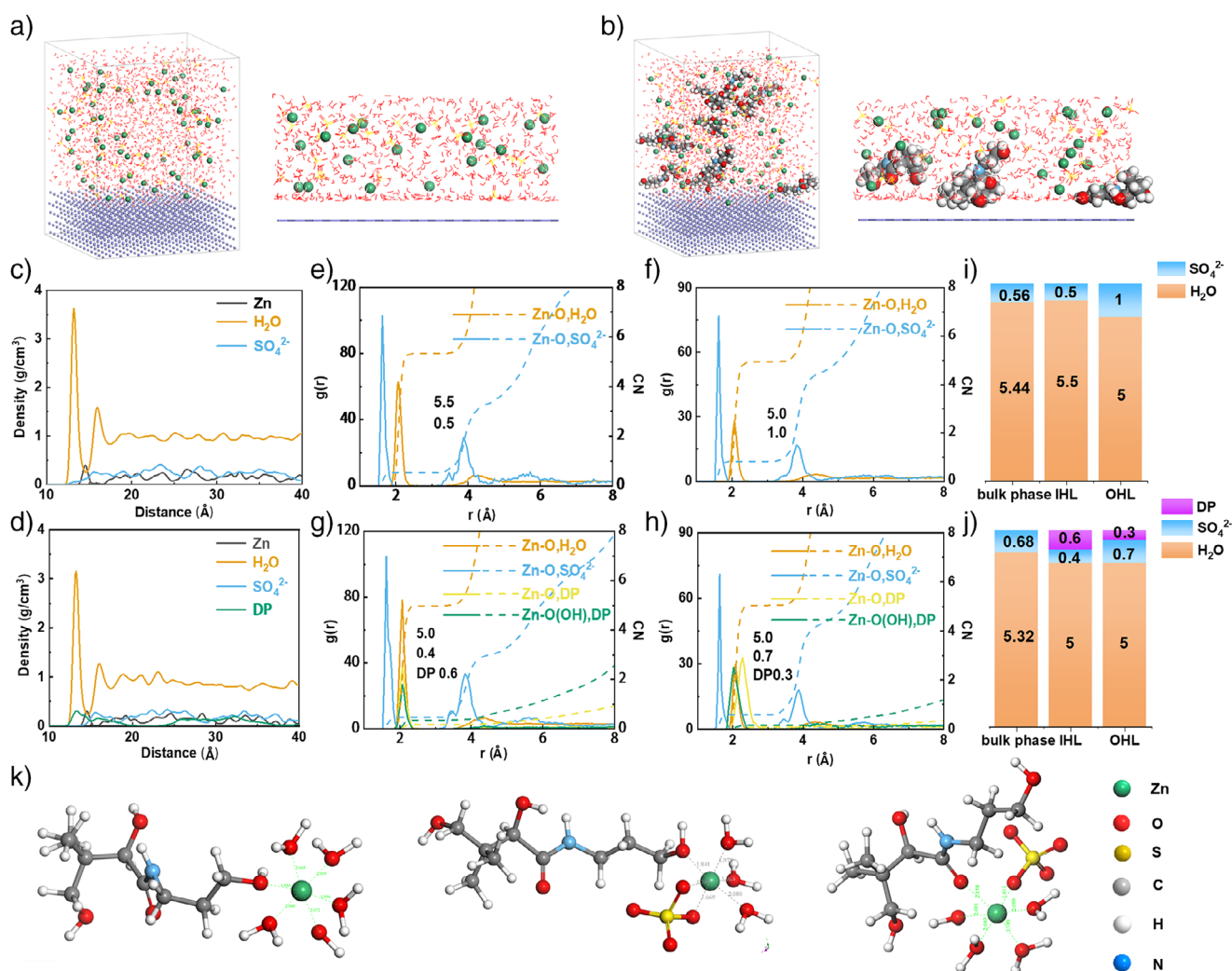
Figure 2. EDL structure and interfacial solvation structure of ZS and ZS-DP electrolytes. a) MD simulation snapshots of EDL structure for Zn anode interface in ZS electrolyte. b) MD simulation snapshots of EDL structure for Zn anode interface in ZS-DP electrolyte. c), d) Normalized density profiles of H_2O, Zn^{2+}, and SO_4^{2-} in the ZS and ZS-DP electrolyte/anode interface along the Z axis. e), f) The RDFs and CN of Zn^{2+}-O in inner EDL and outer EDL of ZS electrolyte. g), h) The RDFs and CN of Zn^{2+}-O in inner EDL and outer EDL of ZS-DP electrolyte. i), j) Comparison between interfacial solvation and bulk solvation structure of ZS and ZS-DP electrolytes. k) Representative Zn^{2+} solvated structure of ZS-DP electrolytes in Helmholtz layer.

Interfacial Solvation Structure

EDL structure and interfacial solvation structure are investigated by electrochemical experiment and MD simulation. As revealed by electrochemical capacitance measurement, ZS-0.05 DP electrolyte exhibits lower EDL capacitance of 61.9 μF·cm^{-2} than that of pure ZS electrolyte (157.0 μF·cm^{-2}), which indicates the DP molecules enter into EDL due to the strong adsorption of DP toward Zn anode (Figure S9). As further visualized by MD simulation, DP molecule tends to migrate from bulk electrolyte to Zn anode interface (Figure S10). Figure 2a,b show the snapshot of simulated

identical (Figure 1g,i). Therefore, Zn^{2+} solvation structure of bulk electrolyte remains unchanged, which contains 5.4 H_2O molecules and 0.6 SO_4^{2-} (Figure S8).

EDL structure and the cross-sectional image of Helmholtz layer region of ZS and ZS-0.05 DP electrolyte. For ZS electrolyte, a large number of water molecules are observed in the IHL (Figures 2a and S11), while hydrated Zn^{2+} and SO_4^{2-} anions are mainly distributed in OHL. Regarding ZS-0.05 DP electrolyte, DP molecules are enriched in EDL and reconfigure EDL, which manipulates the distribution and chemical environment of H_2O, Zn^{2+}, and SO_4^{2-} simultaneously (Figures 2b and S12). DP molecules with large molecule size not only occupy the position of active water but also confine water activity via multifunctional groups, thus suppressing water-related side reactions. Moreover, the normalized density profiles are also performed to quantitatively elucidate the concentration distribution of electrolyte components. As depicted in Figure 2c, IHL possesses the higher H_2O content than OHL, IHL is composed of water dipoles and trace SO_4^{2-} anions, while hydrated Zn^{2+} ions

can approach the edge of IHL and are mainly distributed in the OHL accompanied with most of SO_4^{2-} anions for charge balance. As revealed by the density profiles of ZS-DP electrolytes (Figure 2d), DP molecules substantially reduce the concentration of active water and deliver the gradient distribution from the IHL to OHL. And SO_4^{2-} anions are excluded from IHL by DP molecules and almost entirely distributed in the OHL, while Zn^{2+} ion are enriched in the OHL due to the strong interactions between Zn^{2+} and multifunctional groups of DP molecules.

The EDL reconfiguration significantly modulates the Zn^{2+} interfacial solvation shell environment, as evidenced by RDF and CN in the IHL and OHL. In the IHL of ZS electrolyte, Zn^{2+} is coordinated to 5.5 H_2O molecules and 0.5 SO_4^{2-}, where the existence of rich active-water and non-negligible SO_4^{2-} will accelerate interfacial parasitic side reactions (Figure 2e). While the Zn^{2+} interfacial solvation shell of OHL is composed of 5 H_2O molecules and 1 SO_4^{2-}, and anion-rich solvation restrains Zn^{2+} transfer, thus resulting in poor rate performance (Figure 2f). As highlighted by Figure 2g, the Zn^{2+} interfacial solvation structure is different with bulk solvation structure, which suggests the extreme necessity of investigating and manipulating the interface solvation structure. As for ZS-0.05 DP electrolyte, OH(O) and C=O (O) are analyzed for solvation investigation due to the multifunctional group of DP additive. Interestingly, DP molecules participate in Zn^{2+} solvation coordination, and Zn^{2+} interfacial solvation shell comprises 5.0 H_2O molecules, 0.4 SO_4^{2-} and 0.6 DP in the IHL, where the DP-involved and H_2O/anion-less solvation structure is critical for enhancing interfacial stability and tailoring interfacial chemistry. In the OHL, the CN of H_2O, SO_4^{2-}, and DP is 5.0, 0.7 and 0.3, where the positively charged Zn^{2+} solvation facilitates Zn^{2+} motion in an electric field for fast interface dynamics (Figure 2h). The unique Zn^{2+} interfacial solvation shell is also confirmed by the zeta potential (Figure S13). Moreover, the comparison between interfacial solvation and bulk solvation structure suggests the multifunctional group additive can tailor interfacial solvation structure even at extremely low concentration (Figure 2i–k).

The reconstructed EDL and the unique interfacial solvation structure are mainly attributed to the preferential adsorption of DP toward Zn anode as well as the cooperative interactions between the adsorbed DP with $Zn^{2+}/H^+/H_2O$. Density functional theory (DFT) calculation is performed to investigate the adsorption energy and configuration of H_2O and DP toward Zn anode (Figures 3a,b and S14). The much higher adsorption energies of DP toward Zn anode than that of H_2O molecule suggests that DP molecules are preferentially attached to Zn anode surface to reconstruct EDL structure for suppressing HER and chemical corrosion. Moreover, three typical recumbent configurations of DP toward Zn anode exhibit similar adsorption energies, which indicates no obvious preferred adsorption configuration of DP molecules due to their high molecular chain flexibility and multifunctional groups. The charge density difference of DP-adsorbed Zn anode and the corresponding sliced 2D contour map reveal significant electron transfer between DP

and Zn, which mainly occurs through the polar functional groups such as C=O and OH groups (Figure S15), thus inducing strong chemical adsorption of DP molecule toward Zn anode. Moreover, the intermolecular interactions between the absorbed DP molecule and between $H^+/H_2O/Zn^{2+}$ are investigated by DFT calculations. As evidenced by the negative binding energy (Figure 3c,d), NH of DP can capture H^+ to offer pH buffering capability to inhibit side reactions, while OH group preferentially bind with H_2O, thereby decreasing the activity interfacial H_2O to suppress HER as well as accelerating Zn^{2+} desolvation. In addition, C=O of DP delivers the adsorption affinity with Zn^{2+}, which selectively guides the Zn^{2+} transfer across the EDL and contributes to the uniform deposition. Therefore, DP can simultaneously interact with $H^+/H_2O/Zn^{2+}$ via its multifunctional groups to foster collaborative interface functions.

The suppressed HER by ZS-DP electrolyte is further confirmed by linear sweep voltammetry (LSV) measurement, and ZS-0.05DP electrolyte drives the onset potential for water reduction from -0.04 V down to -0.24 V (versus Zn^{2+}/Zn) (Figure 3e). Meanwhile, oxygen evolution is also suppressed by DP, as indicated by the increase of oxidation onset potential from 1.96 to 2.30 V, which broadens the electrochemical stability window of aqueous electrolytes (Figure S16). The pH buffering capacity of ZS-DP electrolytes is further substantiated by in situ pH monitoring upon the Zn‖Zn symmetric battery cycling at 1 mA cm^{-2} and 1 mAh cm^{-2} (Figure 3f). The pH values of ZS electrolyte remarkably increase from 3.90 to 4.82 only within initial 4 h and fluctuate up to 5.16 during the subsequent 6 h. The increased pH values can be ascribed to HER, while the fluctuated pH values are attributed to the competing reaction between HER and by-product formation. In sharp contrast, the pH values of ZS-0.05DP electrolyte remain steady during 10-hour plating/striping cycles, which further confirms the DP can act as "proton reservoir" to stabilize interfacial pH, thus suppressing the HER and corrosion side reactions.

Moreover, the enhanced Zn^{2+} deposition kinetics is also supported by the lower activation energy (Ea) of ZS-DP electrolyte calculated through the Arrhenius equation (Figures 3g and S17). It has been demonstrated that Zn^{2+} desolvation process is the rate-determining step for Zn^{2+} deposition kinetics. Therefore, the decreased Ea indicates the faster desolvation of hydrated Zn^{2+} in ZS-DP electrolyte at Zn anode interface, as confirmed by the lower stepwise desolvation energy barrier of ZS-0.05DP electrolyte compared with ZS electrolyte (Figure S18). The enhanced interfacial kinetics in ZS-0.05 DP electrolyte is further verified by the distribution of relaxation time (DRT) analysis, where ZS-0.05DP electrolyte affords the shorter relaxation time in relative to ZS electrolyte (Figure S19). In addition, Zn^{2+} transference number is calculated by Bruce–Vincent method, which increases significantly from 0.27 in ZS electrolyte to 0.78 in ZS-DP electrolyte, thus homogenizing Zn^{2+} flux and suppressing Zn dendrites (Figures 3h and S20). The Walden plot also clearly shows that the introduction of DP molecules effectively optimizes the ionicity state of electrolyte and the related ion transport behavior (Figure S21).
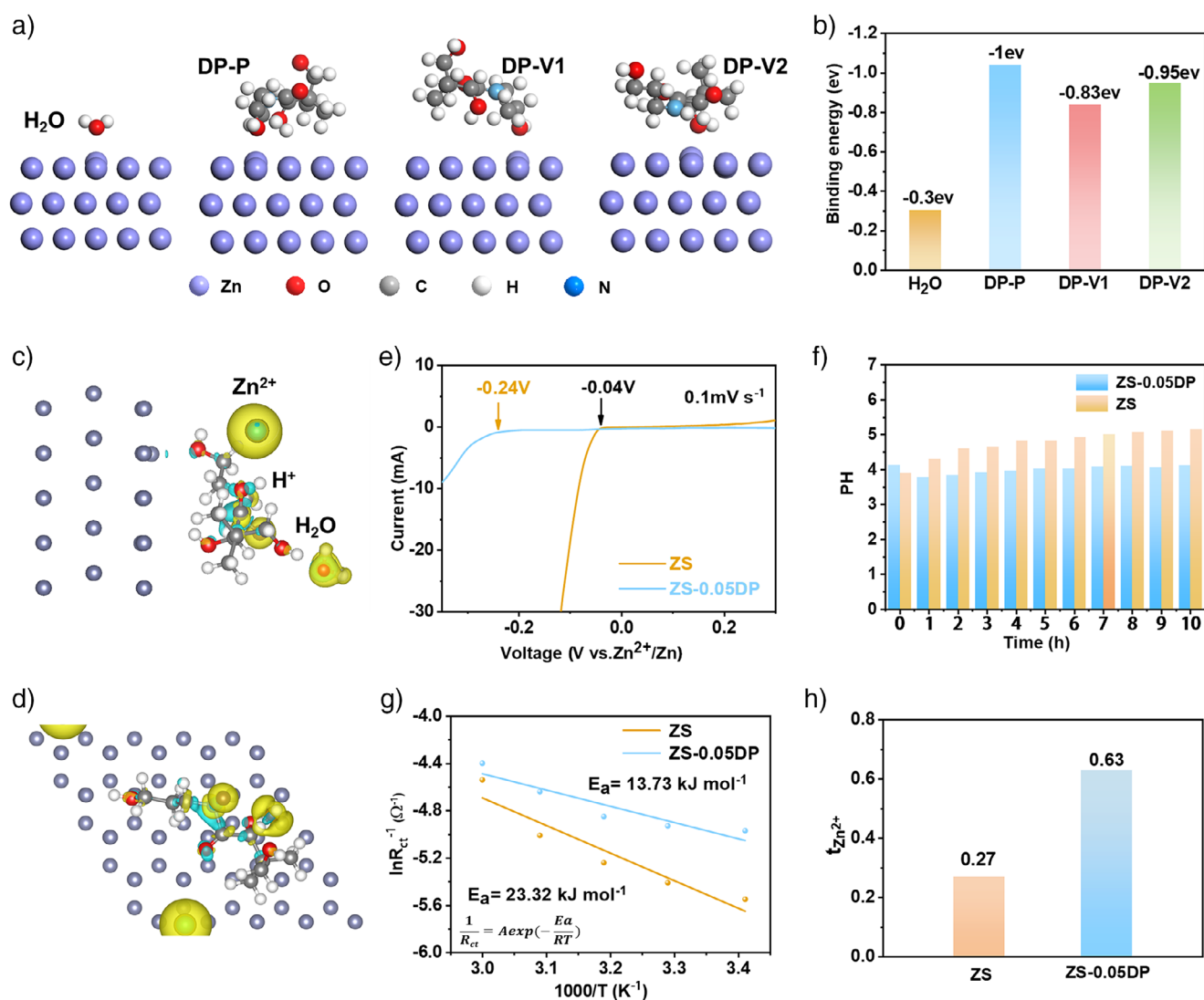
Figure 3. Interfacial interactions and functions. a), b) Adsorption energy and configuration of H_2O and DP toward Zn anode. c), d) Interactions of DP modified Zn anode with Zn^{2+}, H_2O and H^+ indicated by charge density difference. e) HER potential of ZS and ZS-DP electrolytes measured by linear sweep voltammetry. f) In situ pH monitoring of ZS and ZS-0.05DP electrolytes. g) Comparison of activation energies of ZS and ZS-0.05DP electrolytes calculated by the Arrhenius equation. h) Zn^{2+} transfer number of ZS and ZS-0.05DP electrolytes.

Chemistry and Structure of SEI

X-ray photoelectron spectroscopy (XPS) with in-depth profiles and time of flight secondary ion mass spectroscopy (TOF-SIMS) are performed to gain insights into the structure and chemistry of Zn anode after 30 cycles at 0.5 mA·cm^{-2} and 0.5 mAh·cm^{-2} in ZS and ZS-0.05DP electrolytes. XPS survey spectra of Zn anode cycled in ZS-0.05DP electrolyte indicates the existence of C, N, O, S, and Zn on the interface, which signifies DP can effectively tailor the interface chemistry (Figure S22). In the high-resolution C1s spectra (Figure 4a), three characteristic peaks of C—H (284.7 eV), C—O/C=O (286.5 eV), and $ZnCO_3$ (289.5 eV) appear on the Zn anode surface, and C1s signals quickly decrease with increase of the etching depth, especially for organic species. Additionally, N1s spectra also confirm the presence of C—N organic species at 398 eV, which stems from DP molecules. As for

the O1s spectra, only SO_4^{2-} and $Zn(OH)_2$ peaks from byproducts are detected with ZS electrolyte, and the signals of SO_4^{2-} and $Zn(OH)_2$ are still present even after etching for 10 min, which suggests the continuous side reactions (Figure S23). In contrast, three main components of $Zn(OH)_2$ (530.2 eV), C—O/C=O (531.2 eV), and $ZnCO_3$ (532.3 eV) are observed on Zn anode cycled in ZS-0.05DP electrolyte, being consistent with the C1s spectra. Obviously, ZS-0.05DP shows a significant decrease in $Zn(OH)_2$ content, which suggests the suppressed side reactions. Moreover, S2p spectra witness the typical characteristic peaks of $ZnSO_4$ (169.4 eV) and a small amount of ZnS (162.1 eV) with ZS electrolyte, while the Zn anode cycled in ZS-0.05DP electrolyte exhibits higher ZnS proportion. Zn2p spectra confirm the presence of both Zn^{2+} and Zn in the interface, and ZS-DP electrolyte endows the Zn anode interface with more Zn element content, epically in the sublayer. Moreover, the significantly
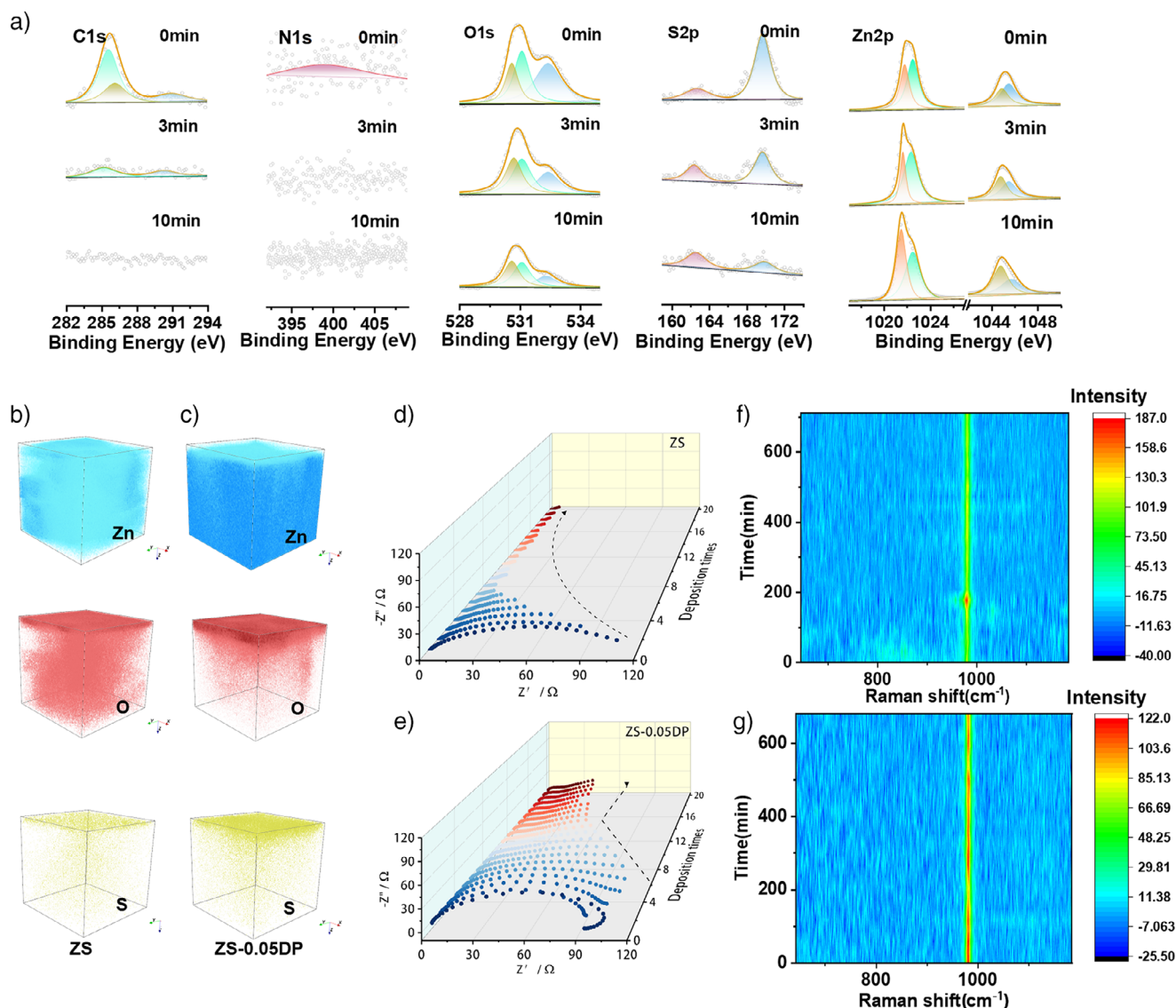
Figure 4. Structure and chemistry of SEI. a) Zn2p, C1s, N1s, S2p, O1s XPS spectra of Zn anode after 30 cycles in ZS-0.05DP electrolyte with different etching time of 0, 3, and 10 min. b), c) Three-dimensional spatial distribution of elements of Zn anode after 30 cycles in ZS and ZS-0.05 DP electrolytes revealed by TOF-SIMS. d), e) In situ EIS of Zn||Zn symmetric batteries using ZS and ZS-0.05DP electrolytes during Zn^{2+} plating. f), g) In situ SERS of SO_4^{2-} intensity changes on Cu working electrode in ZS and ZS-0.05DP electrolytes within the voltage window of -0.8 to -1.5 V (versus Hg/Hg_2SO_4).

enlarged Deger–Aguning–Muller–Tobolov (DMT) modulus of the SEI in ZD-0.05DP electrolyte provides direct evidence of a mechanically robust interface capable of physically suppressing dendrite growth (Figure S24). Therefore, the DP-involved and H_2O/anion-less interfacial solvation structure contributes to formation of organic-inorganic hybrid SEI with organic-rich upper layer and inorganic-rich sublayer, which effectively suppress side reactions and favor the uniform Zn^{2+} deposition.

The interfacial chemistry is further characterized by TOF-SIMS, intuitively presenting 3D reconstructed images of Zn, O, S, C, and N substances (Figures S25 and S26). In ZS electrolyte (Figure 4b), 3D rendering overlay image of elements confirms the messy element distribution and non-uniform Zn deposition, and presence of O and S elements

throughout the detection depth of Zn anode strongly confirms severe side reactions and formation of by-products. In ZS-DP electrolyte (Figure 4c), a clear SEI layer is observed from the elemental spatial mapping, which contributes to the uniform and dense Zn deposition, as evidenced by homogeneous Zn distribution. O and S elements concentrate uniformly at the Zn anode surface, and distinct distribution of N and C elements from DP molecule appears in the sputtering box, collectively indicating a hybrid SEI composition (Figure S27).

The hybrid SEI effectively improves the interfacial electrochemical stability, as visualized by in situ EIS of symmetric batteries during the continuous Zn^{2+} plating. As depicted in Figure 4d, the impedance of Zn anode with ZS electrolyte decreases as the plating time increases, which indicates the dendrite growth forms fresh deposition sites for accelerating

interface deterioration. On the contrary, the impedance gradually decreases within initial deposition process and remains stable throughout subsequent deposition, confirming that the ZS-0.05DP electrolyte assures ultra-stable electrochemical interface and uniform deposition (Figure 4e). Furthermore, in situ surface-enhanced Raman spectroscopy (SERS) illustrates highly reversible plating/stripping processes in ZS-0.05DP electrolyte on account of the hybrid SEI. In ZS electrolyte, SO_4^{2-} stretching vibration exhibits the gradual attenuation, which suggests the accumulation of the by-products (Figure 4f). The HER induces the accumulated OH- on Zn anode, which consumes SO_4^{2-} to form by-products. In contrast, SO_4^{2-} vibration intensity in ZS-0.05DP is potential-dependent and reversibly weakens and intensifies during plating/ striping cycles (Figure 4g), which is indicative of minimized interfacial disturbances during Zn^{2+} plating/striping and obviously ameliorated interfacial reversibility.

High Reversibility of Zn Anode

Zn^{2+} deposition behavior under the unique interfacial solvation microenvironment is investigated by in situ characterization and electrochemical experiments. As monitored by in situ optical microscopy (Figure 5a), deposition in ZS electrolyte for 30 min at a current density of 2 mA cm^{-2} reveals uneven zinc plating and protrusions on the Zn anode, which gradually developed into dendrites with further plating. In contrast, Zn^{2+} plating in the ZS-0.05DP electrolyte is smooth and uniform without visually observing Zn dendrites. Moreover, Zn^{2+} deposition is further investigated by cyclic voltammetry (CV) and chronoamperometry (CA) measurements. As measured by CV curves, ZS-0.05DP electrolyte delivers larger nucleation overpotential compared with the ZS electrolyte, which stems from the synergistic effect of unique interfacial solvation and hybrid SEI, thus contributing to smaller and denser crystal nuclei (Figure S28). CA curves of Zn anode in ZS and ZS-DP electrolytes are also examined under a constant overpotential (-150 mV), where a typical 2D diffusion process is observed in ZS electrolyte with increasing current density, which is conducive to Zn^{2+} local growth and dendrite formation. In sharp contrast, the ZS-0.05DP electrolyte exhibits a consistent 3D diffusion behavior after initial nucleation, thus fostering the uniform Zn deposition (Figure S29). Furthermore, scanning electron microscopy (SEM) and optical microscopy (OM) are also further to intuitively observe Zn^{2+} nucleation morphology in the different electrolytes (Figures S30 and S31). In ZS electrolyte, Zn^{2+} preferentially nucleates in local regions with high activity to form few crystal nuclei with larger sizes, which induces uncontrolled electronic/ionic field on interface and more Zn^{2+} accumulates on them due to the "tip effect", thus eventually leading to fatal dendrite formation. Whereas the ZS-0.05DP electrolyte exhibits denser nucleation sites and smaller sizes, followed by the uniform growth, thus gradually generating even and dense Zn deposition layer.

The interface stability and morphology evolution of Zn anode during cycling are characterized by SEM. After soaking in ZS electrolyte for 10 days, Zn anode shows obvious $Zn_4SO_4(OH)_6 \cdot H_2O$ by-products with randomly oriented hexagonal micro-sheets (Figure S32). However, ZS-DP electrolyte affords interface stability, as evidenced by the smooth Zn anode surface without by-products. Zn anodes after cycling in ZS electrolyte suffer from severe perforation and are covered by numerous Zn protrusions and irregular flake-like dendrites as the cycling proceeds (Figures 5b and S33), indicating the rather uneven Zn^{2+} plating/striping and constant side reactions. Furthermore, a significant amount of residual glass fibers is observed, indicating deposited Zn gradually permeates separator to induce short-circuit. In contrast, Zn anode in ZS-0.05DP electrolyte is more compact and uniform even after 100 cycles, evidencing the homogenous and dendrite-free Zn^{2+} plating/striping. Moreover, 3D microstructure of Zn anodes after 30 cycles in ZS electrolyte and ZS-DP electrolytes were studied using focused ion beam scanning electron microscopy (FIB-SEM). The cycled Zn anode in ZS electrolyte exhibits the porous and irregular structure with the deposition layer thickness of 323.7 nm (Figure 5c), which suggests the disorder deposition and large volume expansion. Fortunately, ZS-0.05DP electrolyte provides Zn anode with a uniform and dense microstructure, which possesses dense deposition layer with high packing density (80.94 nm). Confocal laser scanning microscopy (LCSM) is performed to clearly reveal the 3D surface topology of Zn anodes after 30 cycles in ZS and ZS-DP electrolytes. The color variations with a height difference of 40 μm indicate that deep voids and high protrusions appear on the Zn anode surface in ZS electrolyte, while in ZS-0.05DP electrolyte, the Zn anode is remarkably flat without dendrite formation (Figure 5d).

The unique interfacial solvation structure can effectively tailor the crystallographic structure and reorientation of Zn anode, as revealed by X-ray diffraction (XRD) of Zn anode after 10, 30, and 100 cycles. In ZS electrolyte, peaks in the range of 10° to 20° corresponding to $Zn_4(OH)_6SO_4 \cdot xH_2O$ indicate the presence of corrosion and by-products (Figure S34). No by-product peak is observed in ZS-DP electrolyte, demonstrating its inhibitory effect on HER and by-products. Additionally, for Zn anode cycled in ZS electrolyte (Figure 5e), the peak intensity at 43.3° corresponding to the (101) crystal plane consistently remains the highest, indicating that the (101) crystal orientation predominates throughout the cycling process. As cycle increases from 10 cycles to 100 cycles, the peak intensity ratio of $I_{002}:I_{101}$ is only 0.19, 0.27, and 0.43, respectively. In the ZS-DP electrolyte, the peak intensity ratio of $I_{002}:I_{101}$ in the electrolyte gradually increases, which are respectively 0.39, 0.72, and 0.79, indicating that the ZS-DP electrolyte effectively enhances the Zn (002) crystal plane, thus providing optimal constraints on dendritic growth and interfacial side reactions to boost battery stability. The in situ XRD characterization also reaches the same conclusion (Figure S35).

Electrochemical Performance

Zn anode reversibility was evaluated by a series of electrochemical performance measurement of Zn‖Zn and Zn‖Cu batteries. Zn‖Zn symmetric battery with a small amount of

Research Article

Angewandte
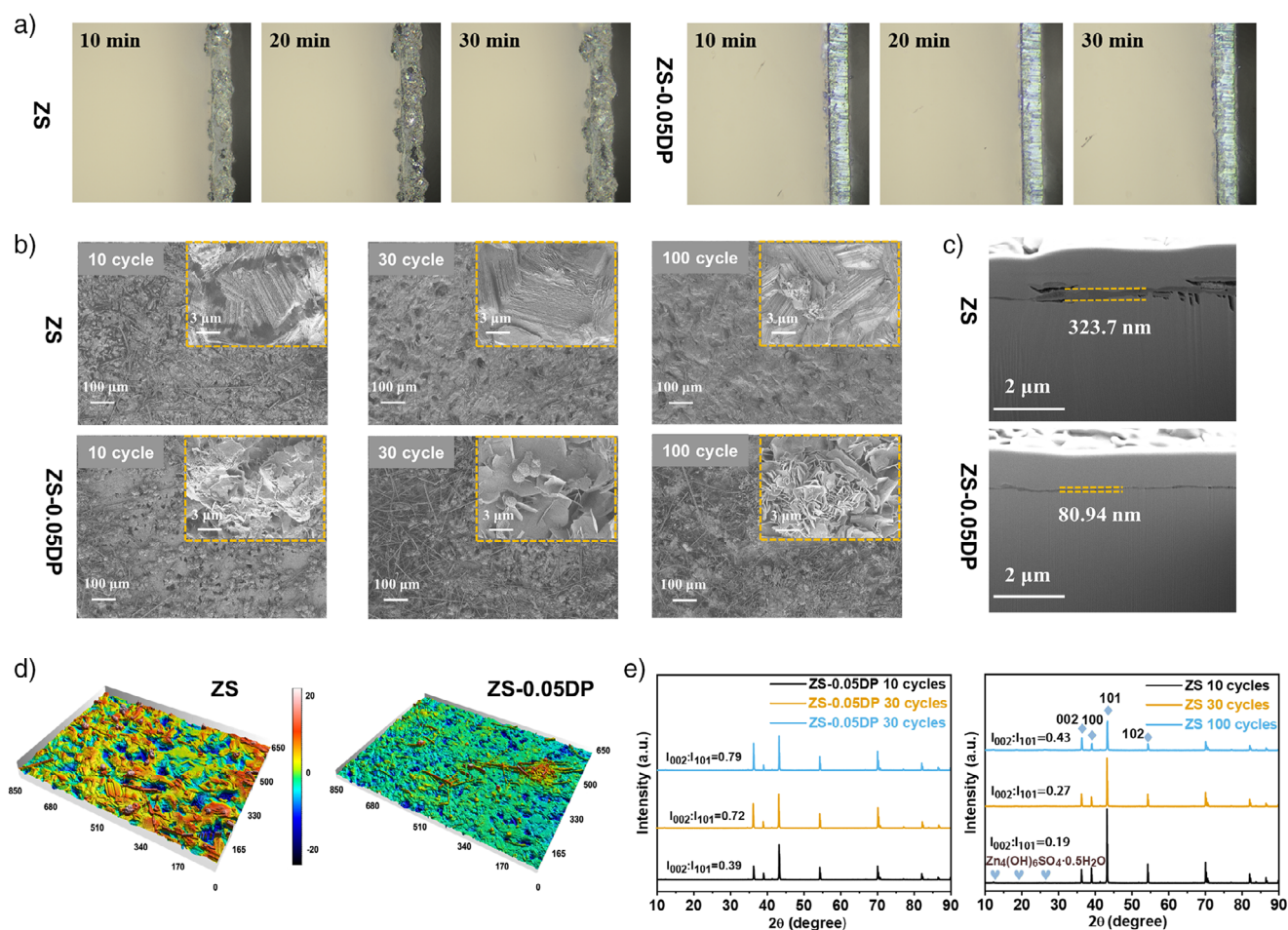*International Edition* *Chemie*

Figure 5. Zn deposition behavior and structure evolution of Zn anode during cycling. a) In situ optical microscope characterization of the Zn deposition in ZS and ZS-0.05DP electrolytes at a current density of 1 mA cm^{-2}. b) SEM images of Zn anodes in ZS and ZS-0.05DP electrolytes after 10 cycles, 30 cycles, 100 cycles at 0.5 mA cm^{-2} and 0.5 mAh cm^{-2}. c) FIB-SEM cross-sectional images of Zn anode after 30 cycles in ZS and ZS-0.05DP electrolytes. d) LCSM images of the Zn anodes after 30 cycles in ZS and ZS-0.05DP electrolytes with a scanning area of 850 μm × 650 μm. e) XRD characterization of Zn anodes in ZS and ZS-0.05DP electrolytes after 10, 30, and 100 cycles under the condition of 0.5 mA cm^{-2} and 0.5 mAh cm^{-2}.

DP additive (0.05 mol L^{-1}) can achieve the longest cycling life of 6700 h (Figure 6a) at current density of 0.5 mA·cm^{-2} and areal capacity of 0.5 mAh·cm^{-2}, while Zn∥Zn symmetric battery with ZS electrolyte is short-circuited after only 230 h (Figure S36). Meanwhile, 1,5-pentanediol, 1,2-pentanediol, N-methylacetamide, and methyl ethyl ketone, which containing only a subset of functional groups in DP molecules such as −OH, amide groups, or carbonyl groups are chosen as additives for the electrolytes. The cycling life of Zn∥Zn symmetric batteries with different additives does not exceed 500 h (Figure S37), which is significantly lower than that of batteries using ZS-DP electrolyte, further demonstrating the synergistic effect of DP's multifunctional groups in enhancing battery performance. And batteries with ZS-0.1DP and ZS-0.5DP electrolytes cycle for 1220 and 1886 h, respectively, which suggests that excessive DP is not conducive to long-term cycling. The high DP content results in the increase of viscosity and interface impedance, which easily trigger the side reactions and uneven Zn^{2+} deposition (Figure S38). Therefore, ZS-0.05 DP electrolyte is selected for further electrochemical measurements. Furthermore, at

high current densities of 1.0 mA·cm^{-2} (1.0 mAh·cm^{-2}), 2.0 mA·cm^{-2} (2.0 mAh·cm^{-2}), 5.0 mA·cm^{-2} (2.0 mAh·cm^{-2}) and 10.0 mA·cm^{-2} (2.0 mAh·cm^{-2}), Zn∥Zn symmetric batteries in ZS-0.05 DP electrolyte exhibit stable cycling for more 5200, 4230, 3216, and 1220 h, which underscores the good ability of DP to enhance Zn anode reversibility (Figure S39). Even at large area capacity of 5.0 mAh·cm^{-2} (5.0 mA cm^{-2}), Zn∥Zn battery has demonstrated a cycling stability over 1179 h, while the battery in ZS electrolyte last only100 h with noticeable increase of polarization voltage (Figure S40). More attractively, the symmetric battery in ZS-0.05DP electrolyte still maintains excellent cycling for 594 h at a high DOD of 85%. However, the symmetric battery in ZS electrolyte experiences a significant voltage fluctuation for 25 h before battery failure (Figure 6b).

Good rate performance is also observed for Zn∥Zn symmetric battery with ZS-DP electrolyte with current density varying from 0.5 to 10 mA·cm^{-2} (Figure S41). Moreover, rate performance under temperature range of 25 to −20 °C reveals the low-temperature self-adaptation of ZS-DP electrolyte, which affords the stable operation
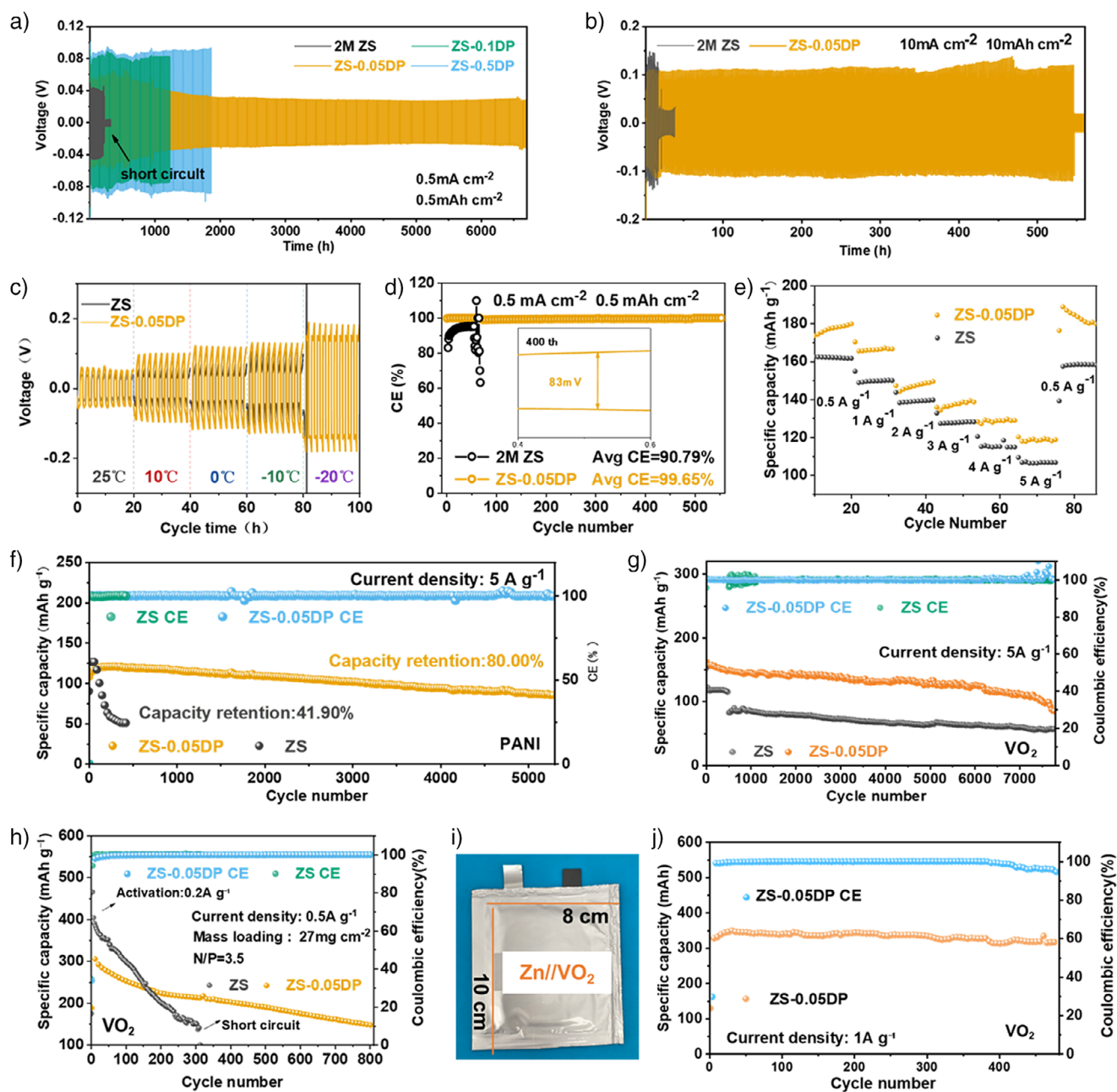
Angew. Chem. Int. Ed. **2025**, e202518035 (9 of 13)

© 2025 Wiley-VCH GmbH

Figure 6. Electrochemical performance. a) Cycling performance of Zn‖Zn symmetric batteries with different ZS-DP electrolytes at 0.5 mA cm^{-2} and 0.5 mAh cm^{-2}. b) Cycling performance of Zn‖Zn symmetric batteries with ZS-0.05 DP electrolyte at high DOD of 85% (10 mA cm^{-2}, 10 mAh cm^{-2}, 20 μm Zn anode). c) Rate performance of Zn‖Zn symmetric batteries with ZS and ZS-0.05DP electrolytes from 25 to -20 °C. d) CE of Zn‖Cu batteries with ZS and ZS-0.05DP electrolytes. e) Rate performances of Zn‖PANI batteries at the current density range from 0.5 to 5 A g^{-1}. f) Long-term cycling stability of Zn‖PANI batteries at a current density of 5 A g^{-1}. g) Long-term cycling stability of Zn‖VO$_2$ batteries at a current density of 5 A g^{-1}. h) Long-term cycling stability of Zn‖VO$_2$ batteries with mass loading of 27 mg cm^{-2} and limited N/P ratio of 3.5 at a current density of 0.5 A g^{-1}. i), j) Image of large-size pouch cell and cycling performance of Zn‖VO$_2$ pouch cell at a current density of 1 A g^{-1}.

of battery at -20 °C (Figure 6c). In contrast, the Zn‖Zn symmetric cell with ZS electrolyte can only operate at -10 °C. Zn‖Zn symmetric battery with ZS-DP electrolyte displays a stable cycling duration of 1200 h at -20 °C (Figure S42), further demonstrating the expanded operating temperature by trace DP additive. Moreover, CE of Zn plating/stripping was assessed in Zn‖Cu asymmetric batteries (Figure 6d). When using ZS electrolyte, Zn‖Cu battery delivers a CE

of 90.79% and cycles for only 65 cycles. In stark contrast, Zn‖Cu battery employing ZS-0.05DP electrolyte exhibits a higher CE of 99.65% with an extended life span of 560 cycles. Notably, ZS-0.05DP electrolyte achieves leading-edge cycling reversibility compared with previous reports (Figure S43), further highlighting the substantial improvement of DP-involved unique interfacial solvation structure on the Zn anode reversibility.

To further validate the feasibility of ZS-DP electrolyte, polyaniline (PANI) and vanadium dioxide (VO_2) have been chosen as the cathode for assembling the Zn‖PANI battery and Zn‖VO_2 cell, respectively. CV curves of Zn‖PANI full battery show the overlapped profiles and similar redox peaks in ZS and ZS-DP electrolytes, indicating the unchanged redox reactions of cathode (Figure S44). As shown in Figures 6e and S45, ZS-DP electrolyte endows Zn‖PANI battery with better rate performance with higher discharge capacity due to the optimized electrode interface. The discharge specific capacity of Zn‖PANI battery with ZS-DP electrolyte is 177.6, 166.0, 146.0, 136.1, 127.1, and 118.2 mAh·g^{-1} at various current densities of 0.5, 1, 2, 3, 4, and 5 A g^{-1}, respectively. When the current density returns to 0.5 A g^{-1}, the actual capacity remains at 177.8 mAh g^{-1} with almost no capacity loss. Moreover, Zn‖PANI battery assembled with the ZS-DP electrolyte exhibits conspicuous cycling performance compared to the ZS electrolyte. The battery with ZS-DP electrolyte retains 80% of its initial capacity after 5300 cycles at 5 g^{-1}, whereas the battery with ZS electrolyte delivers a capacity retention rate of only 41.9% after only 432 cycles due to inherent hydrogen evolution and side reactions (Figure 6f). Even at low temperature of -20 °C, ZS-DP electrolyte can still support the long-term cycling performance of the Zn‖PANI full battery, as evidenced by the stable cycling over 780 cycles without capacity fading (Figure S46). Furthermore, the intercalation material VO_2 was also utilized as the cathode, and the assembled Zn‖VO_2 battery exhibits stable cycling performance for almost 8000 cycles at 5 A g^{-1} in the ZS-DP electrolyte (Figure 6g). To further evaluate the performance at practical condition, Zn‖VO_2 battery was tested with a high active material mass loading (27 mg cm^{-2}) and limited N/P ratio of 3.5, the battery using the ZS-DP electrolyte delivers a superhigh initial surface capacity of 8.1 mAh·cm^{-2} and remains stable over 800 cycles with capacity retention of 50% (Figure 6h). Finally, Zn‖VO_2 pouch batteries with ZS-DP electrolyte delivered an initial capacity of 324 mAh and maintained stable operation over 475 cycles at 1 A g^{-1}, thus validating the feasibility and application potential of the ZS-DP electrolyte in AZMBs for practical energy storage applications (Figure 6i,j and Table S2).

Conclusion

In summary, this study understands the interfacial solvation structure in the EDL, and proposes an efficient multi-group synergy strategy for precisely regulating the interfacial solvation structure. Combined experiments and theoretical simulations highlight solvation structure evolution from bulk electrolyte to EDL and the underlying synergistic mechanism. The preferential adsorption of trace multifunctional group biomolecular DP additive toward Zn anode and the interfacial interactions between H$^+$/H$_2$O/Zn^{2+} and multifunctional groups of DP additives reconstruct EDL and contribute to the formation of unique interfacial solvation structure. Remarkably, positively charged Zn^{2+} interfacial solvation shell in OHL and additive-involved and H$_2$O/anion-less interfacial solvation shell in IHL are formed, which prompts

the formation of stable organic-inorganic hybrid SEI and fosters collaborative interface functions. The unique interfacial solvation structure can synchronously suppress HER, accelerate desolvation kinetics, offer pH Buffering capacity, regulate Zn deposition with crystallographic orientation, which affords long-lifespan Zn anode under high DOD and low temperature. Zn anodes deliver high CE of 99.65%, long-lifespan over 6500 h, and stable operation under low temperature of -20 °C and high DOD of 85.4%. Zn‖PANI full batteries demonstrate the stable cycling over 5300 cycles at 5 A g^{-1}. Furthermore, under high active material mass loading (27 mg cm^{-2}) and limited N/P ratio of 3.5, the Zn‖VO_2 battery remains stable over 800 cycles with capacity retention of 50%, and Zn‖VO_2 pouch batteries can stably operate for almost 500 cycles, demonstrating the practicality of the electrolyte. The pioneering attempt of interfacial solvation structure and the related regulation methodology provides a new perspective for developing high-performance batteries.

Supporting Information

Supporting Information is available from the Wiley Online Library or from the author.

Conflict of Interests

The authors declare no conflict of interest.

Data Availability Statement

The data that support the findings of this study are available from the corresponding author upon reasonable request.

Keywords: Aqueous zinc-ion batteries · Double electric layer · Interfacial solvation structure · Molecular dynamics simulation · Multifunctional interface

Angew. Chem. Int. Ed. **2025**, e202518035 (11 of 13)

© 2025 Wiley-VCH GmbH

[1] C. Wang, B. Chen, T. Wang, G. V. D. O. Silva, Z. Xu, G. X. Miao, Y. Huang, J. Fu, *Energy Environ. Sci.* **2024**, *17*, 11.

[2] H. Wu, S.-J. Zhang, J. Vongsvivut, M. Jaroniec, J. Hao, S.-Z. Qiao, *Joule* **2025**.

[3] P. Xue, C. Guo, W. Gong, Y. Chen, X. Chen, X. Li, J. Yang, Q. Zhang, K. Davey, K. Zhu, *Angew. Chem. Int. Ed.* **2025**, *64*, e202500295, https://doi.org/10.1002/anie.202500295.

[4] Z. Peng, S. Li, L. Tang, J. Zheng, L. Tan, Y. Chen, *Nat. Commun.* **2025**, *16*, 4490, https://doi.org/10.1038/s41467-025-59830-y.

[5] Y. Wang, B. Liang, D. Li, Y. Wang, C. Li, H. Cui, R. Zhang, S. Yang, Z. Chen, Q. Li, *Joule* **2025**, *9*.

[6] S. Wang, N. Ma, P. Zhang, H. Hong, Q. Li, Q. Nian, Y. Wang, Z. Wu, J. Zhu, S. Wang, *J. Am. Chem. Soc.* **2025**.

[7] Y. Song, M. Chen, Z. Zhong, Z. Liu, S. Liang, G. Fang, *Nat. Commun.* **2025**, *16*, 3142, https://doi.org/10.1038/s41467-025-58153-2.

[8] G. Lai, Z. Zhao, H. Zhang, X. Hu, B. Lu, S. Liang, J. Zhou, *Nat. Commun.* **2025**, *16*, 2194, https://doi.org/10.1038/s41467-025-57579-y.

[9] X. Hu, H. Dong, N. Gao, T. Wang, H. He, X. Gao, Y. Dai, Y. Liu, D. J. Brett, I. P. Parkin, *Nat. Commun.* **2025**, *16*, 2316, https://doi.org/10.1038/s41467-025-57666-0.

[10] R. Wang, J. Zhu, M. Yang, Z. Niu, *Angew. Chem. Int. Ed.* **2025**, *137*, e202501327, https://doi.org/10.1002/ange.202501327.

[11] B. Zhang, J. Yao, C. Wu, Y. Li, J. Liu, J. Wang, T. Xiao, T. Zhang, D. Cai, J. Wu, *Nat. Commun.* **2025**, *16*, 71, https://doi.org/10.1038/s41467-024-55657-1.

[12] W. Deng, Z. Deng, Y. Chen, R. Feng, X. Wang, *Angew. Chem. Int. Ed.* **2024**, *63*, e202316499, https://doi.org/10.1002/anie.202316499.

[13] M. Xu, B. Zhang, Y. Sang, D. Luo, R. Gao, Q. Ma, H. Dou, Z. Chen, *Energy Environ. Sci.* **2024**, *17*, 8966–8977, https://doi.org/10.1039/D4EE02815E.

[14] C. Yang, J. Xia, C. Cui, T. P. Pollard, J. Vatamanu, A. Faraone, J. A. Dura, M. Tyagi, A. Kattan, E. Thimsen, *Nat. Sustain.* **2023**, *6*, 325–335, https://doi.org/10.1038/s41893-022-01028-x.

[15] Y.-M. Li, W.-H. Li, K. Li, W.-B. Jiang, Y.-Z. Tang, X.-Y. Zhang, H.-Y. Yuan, J.-P. Zhang, X.-L. Wu, *J. Am. Chem. Soc.* **2024**, *146*, 30998–31011.

[16] H. Dou, X. Wu, M. Xu, R. Feng, Q. Ma, D. Luo, K. Zong, X. Wang, Z. Chen, *Angew. Chem. Int. Ed.* **2024**, *63*, e202401974.

[17] H. Liu, X. Jiang, Z. Hu, Z. Han, J. Chen, K. Bai, Y. Zhang, W. Du, M. Ye, Y. Tang, *Adv. Mater.* **2025**, *37*, 2509622, https://doi.org/10.1002/adma.202509622.

[18] Y. Lv, C. Huang, M. Zhao, M. Fang, Q. Dong, W. Tang, J. Yang, X. Zhu, X. Qiao, H. Zheng, *J. Am. Chem. Soc.* **2025**, *147*, 8523–8533, https://doi.org/10.1021/jacs.4c16932.

[19] M. Yang, S. Bi, X. Wang, Y. Zhang, Y. Hu, J. Tian, L. Liu, Z. Niu, *J. Am. Chem. Soc.* **2025**, *147*, 9294–9303, https://doi.org/10.1021/jacs.4c15126.

[20] R. Zhao, H. Wang, H. Du, Y. Yang, Z. Gao, L. Qie, Y. Huang, *Nat. Commun.* **2022**, *13*, 3252, https://doi.org/10.1038/s41467-022-30939-8.

[21] Y. Chen, S. Zhou, J. Li, J. Kang, S. Lin, C. Han, H. Duan, S. Liang, A. Pan, *Adv. Energy Mater.* **2024**, *14*, 2400398, https://doi.org/10.1002/aenm.202400398.

[22] M. Kim, S. J. Shin, J. Lee, Y. Park, Y. Kim, H. Kim, J. W. Choi, *Angew. Chem. Int. Ed.* **2022**, *134*, e202211589, https://doi.org/10.1002/ange.202211589.

[23] Z. He, L. Pan, Z. Peng, Z. Liu, Z. Zhang, B. Li, Z. Zhang, X. Wu, N. Zhao, L. Dai, *Adv. Energy Mater.* **2025**, *15*, 2403958.

[24] J. Cao, Y. Jin, H. Wu, Y. Yue, D. Zhang, D. Luo, L. Zhang, J. Qin, X. Yang, *Adv. Energy Mater.* **2025**, *15*, 2403175, https://doi.org/10.1002/aenm.202403175.

[25] H. Fu, S. Huang, T. Wang, J. Lu, P. Xiong, K. Yao, J. S. Byun, W. Li, Y. Kim, H. S. Park, *Adv. Mater.* **2025**, *37*, 2411686, https://doi.org/10.1002/adma.202411686.

[26] H. Gan, H. Li, M. Xu, C. Han, H.-M. Cheng, *Joule* **2024**, *8*, 3054–3071, https://doi.org/10.1016/j.joule.2024.07.013.

[27] C. Yan, F. He, L. Feng, L. Zhu, P. Li, J. Tang, H. He, Y. Liu, Y. Zhu, G. Li, *Adv. Funct. Mater.* **2025**, *35*, 2503493, https://doi.org/10.1002/adfm.202503493.

[28] Y. Sang, J. Wang, M. Xu, B. Zhang, Q. Huang, D. Wang, C. Liu, Y. Zhang, H. Dou, Z. Chen, *Angew. Chem. Int. Ed.* **2025**, e202506984.

[29] Z. Zhang, X. Lan, G. Liao, W. Du, Y. Zhang, M. Ye, Z. Wen, Y. Tang, X. Liu, C. C. Li, *Angew. Chem. Int. Ed.* **2025**, *64*, e202503396, https://doi.org/10.1002/anie.202503396.

[30] W. Zhang, S. Zhu, T. Yang, L. Wu, J. Li, J. Liang, Y. Liu, L. Cui, C. Tang, X. Chen, *Angew. Chem. Int. Ed.* **2025**, *64*, e202419732, https://doi.org/10.1002/anie.202419732.

[31] G.-X. Li, P. Lennartz, V. Koverga, R. Kou, A. Nguyen, H. Jiang, M. Liao, D. Wang, N. Dandu, M. Zepeda, *Proc. Natl. Acad. Sci. USA* **2024**, *121*, e2311732121, https://doi.org/10.1073/pnas.2311732121.

[32] N. Li, K. Gao, K. Fan, L. Ma, Z. Li, B. He, C. Shen, Q. Ye, K. Xie, H. Huang, *Energy Environ. Sci.* **2024**, *17*, 5468–5479, https://doi.org/10.1039/D4EE01463D.

[33] J. Wang, J. Luo, H. Wu, X. Yu, X. Wu, Z. Li, H. Luo, H. Zhang, Y. Hong, Y. Zou, *Angew. Chem. Int. Ed.* **2024**, *136*, e202400254, https://doi.org/10.1002/ange.202400254.

[34] Z. Li, Z. Wang, W. Sun, Y. Ma, W. Guo, Y. Fu, *Adv. Mater.* **2025**, *37*, 2420489, https://doi.org/10.1002/adma.202420489.

[35] P. Liang, J. Li, Y. Dong, Z. Wang, G. Ding, K. Liu, L. Xue, F. Cheng, *Angew. Chem. Int. Ed.* **2025**, *64*, e202415853, https://doi.org/10.1002/anie.202415853.

[36] G. Zeng, Q. Sun, S. Horta, P. R. Martínez-Alanis, P. Wu, J. Li, S. Wang, M. Ibáñez, Y. Tian, L. Ci, *Energy Environ. Sci.* **2025**, *18*, 1683–1695, https://doi.org/10.1039/D4EE03750B.

[37] X. Li, S. Wu, L. Qiu, J. Xiang, P. Zeng, X. Wang, D. Xiao, J. Li, P. Li, *J. Colloid Interface Sci.* **2025**, *686*, 960–969, https://doi.org/10.1016/j.jcis.2025.02.026.

[38] P. Wang, Y. Zhong, J. Wang, H. Zhou, G. Sun, X. Sui, Z. Wang, *Adv. Funct. Mater.* **2025**, *35*, 2414563, https://doi.org/10.1002/adfm.202414563.

[39] Y. Liu, Z. Liu, Z. Xiao, Z. Lao, J. Liu, X. Xiao, Q. Fu, F. Zheng, G. Zhou, *Angew. Chem. Int. Ed.* **2025**, *64*, e202502896.

[40] M. Tang, X. Zhao, R. Han, Y. Wang, Y. Ding, Z. Si, B. Li, D. Zhou, F. Kang, *Angew. Chem. Int. Ed.* **2025**, *64*, e202421574, https://doi.org/10.1002/anie.202421574.

[41] S. Yan, H. Liu, Y. Lu, Q. Feng, H. Zhou, Y. Wu, W. Hou, Y. Xia, H. Zhou, P. Zhou, *Sci. Adv.* **2025**, *11*, eads4014, https://doi.org/10.1126/sciadv.ads4014.

[42] C. Li, Y. Liu, J. Liu, M. Liu, Y. Gao, X. Wang, Y. Zheng, J. Liu, L. Ma, L. Ouyang, *J. Am. Chem. Soc.* **2025**, *147*, 27640–27650, https://doi.org/10.1021/jacs.5c06049.

[43] J. Luo, L. Xu, Y. Yang, S. Huang, Y. Zhou, Y. Shao, T. Wang, J. Tian, S. Guo, J. Zhao, *Nat. Commun.* **2025**, *15*, 1–12.

[44] M. Chuai, H. Tong, Z. Yang, S. Deng, M. Wu, J. Xing, G. Chai, *J. Am. Chem. Soc.* **2025**.

[45] J. Yan, H. Dou, M. Su, M. Xu, S. Liu, S. Qin, B. Zhang, K. Zong, L. Tan, X. Wang, *Angew. Chem. Int. Ed.* **2025**, *64*, e202505372, https://doi.org/10.1002/anie.202505372.

[46] S. Tang, Q. Wei, B. Liu, J. Yang, H. Jiang, Y. Ge, D. Wu, J. Li, T. Qiu, H. Zhang, *Angew. Chem. Int. Ed.* **2025**, *64*, e202510252, https://doi.org/10.1002/anie.202510252.

[47] M. Su, H. Dou, J. Yan, S. Liu, M. Xu, C. Liu, X. Wang, Z. Chen, *Angew. Chem. Int. Ed.* **2025**, *64*, e202511685, https://doi.org/10.1002/anie.202511685.

[48] D. M. Markiewitz, Z. A. Goodwin, Q. Zheng, M. McEldrew, R. M. Espinosa-Marzal, M. Z. Bazant, *ACS Appl. Mater. Interfaces* **2025**, *17*, 29515–29534, https://doi.org/10.1021/acsami.5c01781.

[49] T. Shen, T. Wei, S. Zhang, H. Liu, C. Li, Z. Li, M. Yang, C. Liu, Y. Pei, *Small Struct.* **2025**, *6*, 2400325, https://doi.org/10.1002/sstr.202400325.

[50] Z. Fang, J. Li, L. Xiang, K. Liu, Y. Pan, X. Li, D. Lin, K. Zhu, C. Han, Y. Yao, *Energy Storage Mater.* **2025**, *82*, 104592, https://doi.org/10.1016/j.ensm.2025.104592.

[51] P. Zheng, J. Ren, J. Zheng, F. Liu, X. Han, B. Yu, *Metab. Eng.* **2025**, *92*, 63–75, https://doi.org/10.1016/j.ymben.2025.07.013.

[52] S. Garli, Ö. ÖZMEN, Ş. TAŞAN, *Kafkas Üniversitesi Veteriner Fakültesi Dergisi* **2025**, *31*.

[53] X. Xu, X. Xie, A. Pan, H. Duan, G. Fang, S. Liang, *ACS Energy Lett.* **2025**, *10*, 4386–4394, https://doi.org/10.1021/acsenergylett.5c02217.

[54] K. Su, Z. Bian, Y. Mu, Z. Lu, Y. Wang, M. Li, J. Zhao, J. Lang, B. Xu, *Energy Storage Mater.* **2025**, *81*, 104480, https://doi.org/10.1016/j.ensm.2025.104480.

[55] L. Liu, X. Wang, Z. Hu, X. Wang, Q. Zheng, C. Han, J. Xu, X. Xu, H. K. Liu, S. X. Dou, *Angew. Chem. Int. Ed.* **2024**, *63*, e202405209, https://doi.org/10.1002/anie.202405209.

[56] J. Liu, C. Li, Q. Lv, D. Chen, J. Zhao, X. Xia, Z. Wu, J. Lai, L. Wang, *Adv. Energy Mater.* **2024**, *14*, 2401118.

[57] H. Lyu, S. Zhao, C. Liao, G. Li, J. Zhi, F. Huang, *Adv. Mater.* **2024**, *36*, 2400976, https://doi.org/10.1002/adma.202400976.

[58] K. Qi, P. Liang, S. Wei, H. Ao, X. Ding, S. Chen, Z. Fan, C. Wang, L. Song, X. Wu, *Energy Environ. Sci.* **2024**, *17*, 2566–2575, https://doi.org/10.1039/D4EE00147H.